Ciliotherapy: Remote Control of Primary Cilia Movement and Function by Magnetic Nanoparticles

Rajasekharreddy Pala[1,2], Ashraf M. Mohieldin[1,2], Rinzhin T. Sherpa[1,2], Sarmed H. Kathem[1,2], Kiumars Shamloo[1,2], Zhongyue Luan[3], Jing Zhou[4], Jian-Guo Zheng[5], Amir Ahsan[6], Surya M. Nauli[*,1,2]

[1]Department of Biomedical & Pharmaceutical Sciences, Chapman University School of Pharmacy (CUSP), Harry and Diane Rinker Health Science Campus, Chapman University, Irvine, California 92618, USA. [2]Department of Medicine, University of California Irvine, Irvine, CA 92868, USA. [3]Chemical Engineering & Material Sciences, University of California Irvine, Irvine, CA 92697, USA. [4]Department of Medicine, Harvard Medical School, Boston, MA 02115, USA. [5]Irvine Materials Research Institute, University of California Irvine, Irvine, CA 92697, USA. [6]Department of Physics, Computer Science & Engineering, Chapman University, Orange, CA 92866, USA

[*]Corresponding author:
Surya M. Nauli
Chapman University
The University of California, Irvine
9401 Jeronimo Road.
Irvine, CA 92618-1908
Tel: 714-516-5480
Fax: 714-516-5481
Email: nauli@chapman.edu; snauli@uci.edu

Table of Contents **Page**

Supporting Movie Legends

Movie 1. Live imaging reveals the specific targeting of the CT-Fe_2O_3-NPs to primary cilia.

A field of view (phase contrast) was randomly selected and recorded while the CT-Fe_2O_3-NPs were introduced to the cell population. The specific targeting of the CT-Fe_2O_3-NPs to primary cilia was visible (red) within 30 minutes. The CT-Fe_2O_3-NPs accumulated in the cilia in a time-dependent manner, as indicated by the increasing fluorescence signal. Arrows (white) indicate primary cilia.

Movie 2. 3D rendering of a primary cilium.

The specific localization of the CT-Fe_2O_3-NPs is shown in red, and the cilia marker acetylated-α-tubulin is shown in green.

Movie 3. Effect of a magnetic field on a cilium targeted by the superparamagnetic Fe_2O_3-NPs.

Single-cell-single-cilium imaging shows that the external magnetic field acting on the CT-Fe_2O_3-NPs (red fluorescence; CT-M-Fe_2O_3-NPs) induced passive cilia movements in a live cell. The magnetic field was oscillating along the cilium.

Movie 4. Intraciliary and cytosolic Ca^{2+} signaling in a PBS-treated control cell challenged with fluid shear stress.

Single-cell-single-cilium imaging of an LLC-PK1 cell expressing 5HT6-mCherry-G-GECO1.0 that was treated with PBS as an experimental control and exposed to shear stress (0.5 dyn/cm2). GECO (green) shows Ca^{2+} signals, mCherry (red) indicates any motion artefacts, the

GECO/mCherry signal was used for visualization purposes, DIC tracked cilia movement, the 4 GECO/mCherry signal was used to label the region of interest, and the GECO/mCherry ratio is used to identify changes in normalized intraciliary Ca^{2+} levels to avoid potential artefacts. Due to cilia movement, binary spotting was used to identify changes in signal intensity along the ciliary shaft. The scale bar represents 5 μm.

Movie 5. Intraciliary and cytosolic Ca^{2+} signaling in a fenoldopam-treated control cell challenged with fluid shear stress.

Single-cell-single-cilium imaging of an LLC-PK1 cell expressing 5HT6-mCherry-G-GECO1.0 that was treated with fenoldopam as an experimental control and exposed to shear stress (0.5 dyn/cm2). GECO (green) shows Ca^{2+} signals, mCherry (red) indicates any motion artefacts, the GECO/mCherry signal was used for visualization purposes, DIC tracked cilia movement, the GECO/mCherry signal was used to label the region of interest, and the GECO/mCherry ratio is used to identify changes in normalized intraciliary Ca^{2+} levels to avoid potential artefacts. Due to cilia movement, binary spotting was used to identify changes in signal intensity along the ciliary shaft. The scale bar represents 5 μm.

Movie 6. Intraciliary and cytosolic Ca^{2+} signaling in a cCT-Fe_2O_3-NP-treated cell challenged with fluid shear stress.

Single-cell-single-cilium imaging of an LLC-PK1 cell expressing 5HT6-mCherry-G-GECO1.0 that was treated with the cCT-Fe_2O_3-NPs and exposed to shear stress (0.5 dyn/cm2). GECO (green) shows Ca^{2+} signals, mCherry (red) indicates any motion artefacts, the GECO/mCherry signal was used for visualization purposes, DIC tracked cilia movement, the GECO/mCherry

signal as used to label the region of interest, and the GECO/mCherry ratio was used to identify changes in 5 normalized intraciliary Ca^{2+} levels to avoid potential artefacts. Due to cilia movement, binary spotting was used to identify changes in signal intensity along the ciliary shaft. The scale bar represents 5 μm.

Movie 7. Intraciliary and cytosolic Ca^{2+} signaling in a CT-Fe_2O_3-NP-treated cell challenged with fluid shear stress.

Single-cell-single-cilium imaging of an LLC-PK1 cell expressing 5HT6-mCherry-G-GECO1.0 that was treated with the CT-Fe_2O_3-NPs and exposed to shear stress (0.5 dyn/cm2). GECO (green) shows Ca^{2+} signals, mCherry (red) indicates any motion artefacts, the GECO/mCherry signal was used for visualization purposes, DIC tracked cilia movement, the GECO/mCherry signal was used to label the region of interest, and the GECO/mCherry ratio was used to identify changes in normalized intraciliary Ca^{2+} levels to avoid potential artefacts. Due to cilia movement, binary spotting was used to identify changes in signal intensity along the ciliary shaft. The scale bar represents 5 μm.

Movie 8. Intraciliary and cytosolic Ca^{2+} signaling in a cCT-M-Fe_2O_3-NP-treated cell exposed to a magnetic field.

Single-cell-single-cilium imaging of an LLC-PK1 cell expressing 5HT6-mCherry-G-GECO1.0 that was treated with the cCT-M-Fe_2O_3-NPs and exposed to an oscillating magnetic field (1.35 T). GECO (green) shows Ca^{2+} signals, mCherry (red) indicates any motion artefacts, the GECO/mCherry signal was used for visualization purposes, DIC tracked cilia movement, the GECO/mCherry signal was used to the label region of interest, and the GECO/mCherry ratio was

used to identify changes in normalized intraciliary Ca^{2+} levels to avoid potential artefacts. Due to 6 potential movement, binary spotting was used to identify changes in signal intensity along the ciliary shaft. Binary spotting was not observed in the negative control. The scale bar represents 5 μm.

Movie 9. Intraciliary and cytosolic Ca^{2+} signaling in a CT-M-Fe_2O_3-NP-treated cell exposed to a magnetic field.

Single-cell-single-cilium imaging of an LLC-PK1 cell expressing 5HT6-mCherry-G-GECO1.0 that was treated with the CT-M-Fe_2O_3-NPs and exposed to an oscillating magnetic field (1.35 T; CT-M-Fe_2O_3-NPs). GECO (green) shows Ca^{2+} signals, mCherry (red) indicates any motion artefacts, the GECO/mCherry signal was used for visualization purposes, DIC tracked cilia movement, the GECO/mCherry signal was used to label the region of interest, and the GECO/mCherry ratio was used to identify changes in normalized intraciliary Ca^{2+} levels to avoid potential artefacts. Due to cilia movement, binary spotting was used to identify changes in signal intensity along the ciliary shaft. The scale bar represents 5 μm.

Movie 10. Speed of a single blood cell in 48-hpf zebrafish.

Blood flow from the dorsal region of the main artery and vein within the medial-posterior lateral trunk are shown in control (scrambled morpholino) and Pkd2 morphants treated with PBS, CT-Fe_2O_3-NPs or CT-M-Fe_2O_3-NPs. A single blood cell was locked-in and automatically traced with the NIS-Elements High Content tracking software; changes in the blood velocity are plotted in line graphs.

Movie 11. Heart rate in 48-hpf zebrafish.

Movies of beating hearts of control (scrambled morpholino) and Pkd2 morphants treated with PBS, CT-Fe_2O_3-NPs or CT-M-Fe_2O_3-NPs are shown. The heart beat profiles were tracked with the NISElements High Content tracking software and are depicted in line graphs.

Movie 12. Working heart system.

This video was captured through the Plexiglas acrylic chamber in which the isolated heart (108 mg) was kept viable for as long as possible by maintaining a constant temperature *via* heat exchangers located in and around the chamber. The temperature, pH and pO2 of the perfusion buffer were independently maintained. The perfusion heads, electrocardiogram detector, transonic flowmeter and pressure electrode are shown in the video.

Mean-field Model of Magnetically Actuated Cilia

A simple mean-field model is considered following Evans *et al.*[1,2] of primary cilia magnetically actuated by an external magnetic field facilitated by the presence of haematite (α-Fe_2O_3) nanoparticles attached to the surface of cilia. At room temperature haematite is weakly ferromagnetic without an external magnetic field and is magnetized in the presence of it. The energy of the magnetic-cilia system consists of elastic and magnetic energy, $H = H_{Elastic} + H_{Magnetic}$. Modeling cilia as a thin elastic cylindrical rod of length L with flexural stiffness EI (E is the Young's modulus of the rod and I is its second moment of inertia), i.e. Kirchoff elastic rod model,[3] attached to an infinite surface with a permanent magnet above cilia, see figure 1, as an external magnetic field source. The bending energy is given by

$$H_E = \frac{1}{2} EI \int_0^L \frac{1}{R^2(s)} ds \tag{1}$$

where we assume a constant radius of curvature $R(s) \approx R$ and parameterize in terms of the angle φ, see figure 1, thus with $R = L/2\varphi$ the elastic contribution simplifies to $H_E = 2EI\varphi^2 / L$. The magnetic energy is

$$H_M = -A \int_0^L \vec{B}(s) \cdot \vec{M}(s) ds \tag{2}$$

where A is the cross-sectional area and $\vec{M}(s)$ is the magnetization along the arclength of the rod and $\vec{B}(s)$ is the total magnetic field due to internal magnetic moment of iron-oxide (Fe_2O_3), $\vec{B}_{in}(s)$, along the arc-length and the field due to the applied field of the magnet $\vec{B}_A(s)$, $\vec{B}(s) = \vec{B}_{in}(s) + \vec{B}_A(s)$. The magnetic energy can thus be viewed as the internal magnetic energy of the rod H_I and that due to the applied magnetic field H_A, $H_{Magnetic} = H_I(B_I) + H_A(B_A)$. Adopting the Stoner-Wolfarth model for the internal magnetic energy of the rod,[4]

$$H_I = \frac{1}{2} \mu_0 \frac{m^2}{V} \left(N_a - N_b \right) \cos^2(\alpha - \varphi) \tag{3}$$

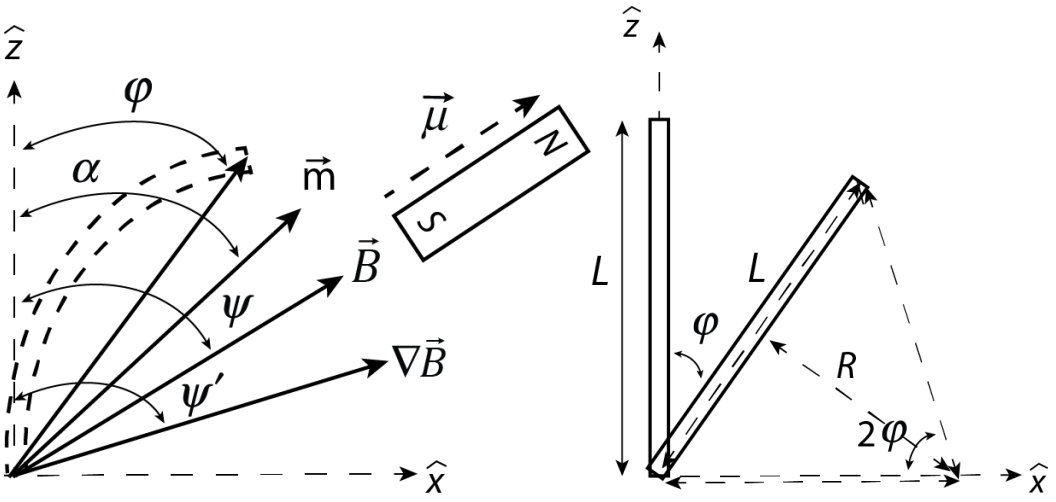

(a) (b)

Figure 1. (a) General directions of the rod φ (bent rod (dashed), arrow represents model), average magnetic moment of the rod ($\vec{m}$), α, the magnetic field ($\vec{B}$), ψ, and it's gradient ($\nabla\vec{B}$), ψ'. Schematic also shown of the external magnet with magnetic moment $\vec{\mu}$. (b) Simplified model of cilia as a rod of length L where R represents the radius of curvature such that $R \approx L/2\varphi$.

where m is net magnetic moment of the rod, angularly displaced by α, and φ is the angular position of the long axis of the rod (see figure 1), V is the volume of the rod and N_a and N_b are the demagnetization factors parallel and perpendicular to the long axis. Given the large aspect ratio of cilium ($L/2a = 21\mu m/200nm \sim 100$) the demagnetization factor can be approximated with $N_a \sim 0$ and $N_b \sim ½$.[3] The magnetic moment of the rod will align with the applied magnetic field to minimize the applied field energy, thus we can let $\alpha = \psi$ and the internal energy reduces to

$$H_I = -\frac{1}{4}\mu_0 \frac{m^2}{V}\cos^2(\psi - \varphi) \tag{4}$$

The energy associated with the applied field is

$$H_A = -A\int_0^L B_A M(B)\, ds \tag{5}$$

where the applied field B_A is nonuniform and is approximated by the first two terms in the Maclaurin series, $B_A \approx B_0 + \nabla B l \cos(\psi' - \varphi)$. The magnetization M(B) is approximated with $M(B) = \chi B_A$, where χ is the magnetic susceptibility, thus the field energy becomes

$$H_A = -A\chi\int_0^L \left[B_0 + (\nabla B)s\cos(\psi' - \varphi)\right]^2 ds \tag{6}$$

Neglecting terms of order $(\nabla Bs)^2$ the applied field energy becomes, after integrating and neglecting the constant term that is independent of the motion of the rod,

$$H_A = -\frac{1}{2} m \nabla BL \cos(\psi' - \varphi) \tag{7}$$

where $m = AL\chi B_0$ is the magnetic moment of the rod and $AL = V$, is the volume of cilium. This represents the attractive interaction of the magnetic moment of the rod and the gradient of the magnetic field. The total energy of the rod, equations (1), (4) and (7) is thus

$$H = \frac{2EI}{L}\varphi^2 - \frac{1}{4}\mu_0 \frac{m^2}{V}\cos^2(\psi - \varphi) - \frac{1}{2} m \nabla BL \cos(\psi' - \varphi) \tag{8}$$

which consists of the elastic and magnetic energy of the rod. The second term represents the internal magnetic energy associated with the misalignment of the rod (φ) from the direction of the magnetic field (ψ), which is minimized when $\psi = \varphi$, favoring the rod to point in the direction of the applied field, thus the field energy term. The last term is the gradient energy term, associated with the attractive interaction of the gradient of the magnetic field of the magnet with the magnetic moment of the cilium-haematite composite and is minimized when $\psi' = \varphi$.

The net torque acting on cilium is $\tau = dH / d\varphi$,

$$\tau = \frac{4EI}{L}\varphi - \frac{1}{2}\frac{\mu_0 m^2}{V}\cos(\psi - \varphi)\sin(\psi - \varphi) - \frac{1}{2} m \nabla BL \sin(\psi' - \varphi) \tag{9}$$

where the magnetic torque associated the field energy term, the second term, is maximized when the angle between the applied field and rod is 45^0, $\psi - \varphi = 45^\circ$, while the torque associated with the gradient energy is maximized when the gradient of the field and rod is 90^0. Given the permanent magnet field source, the field alignment energy will dominate relative to the gradient energy.[1] Thus considering only the elastic and field energy terms in the torque, equation (9), and setting the torque to zero and substituting $m = V\chi B$, we find the magnetic field required to maintain an angular displacement of φ,

$$B = \frac{4}{\chi}\sqrt{\frac{EI}{\mu_0 V}}\varphi^{1/2} \quad . \tag{10}$$

For an angular displacement of π/4 and with length and radius of cilium, *21 μm* and *100 nm*, respectively and susceptibility χ = 0.59 is obtained from a plot of the magnetization as a function

of the applied field for hematite, consistent with that found for haematite at room temperature,[5,6] and setting the rigidity of cilium to be $EI = 3\times10^{-23}\,Nm^2$ the required magnetic field is B ~36 T.

We can estimate the attractive force, $F_z = -dH_A/dz$, assuming the field varies with z. The field energy (4) is minimized when $\psi = \varphi$, thus $H_I = -\mu_0 m^2/4V = -\mu_0 V\chi^2 B^2$. Thus the force is $F_z = -dH_A/dz$,

$$F = \frac{1}{2}\mu_0 V\chi^2 B\frac{dB}{dz} \tag{11}$$

The applied field of the magnet is approximated with the field of a magnetic dipole along the long axis of the magnet and far from the magnet (taken to be the negative z-direction), i.e. $B_z \approx -\mu_0\mu/2\pi z^3$, where μ is the magnet moment of the magnet, and thus the gradient is $\nabla B_z = 3\mu_0\mu/2\pi z^4$. The attractive force due to the field energy of the field is thus

$$F = -\frac{3}{8\pi^2}\frac{\mu_0^3 V\chi^2\mu^2}{z^7}\ . \tag{12}$$

The magnetic moment, μ, of the magnet, an AlNiCo magnet with a length of 3 inches and diameter of .5 inches, is determined from the value of the field at the poles, equal to B = 1.35 T. Given the behavior of the magnetic field of the magnet along the long axis is given by

$$B_{magnet} = \hat{z}\frac{\mu_0\mu}{2V_m}\left[\frac{z+l/2}{\sqrt{a^2+(z+l/2)^2}} - \frac{z-l/2}{\sqrt{a^2+(z-l/2)^2}}\right]$$

where at $z = l/2$, B = 1.35 T, thus corresponding to a magnet moment of the magnet of $\mu = 84\,Am^2$. Thus using this value for the magnetic moment of the magnet and χ = 0.59 the force (12) acting on cilium of length *21 μm* and radius *100 nm* is $F \sim .1pN$ when z = 1mm. This is comparable to the force needed to bend a cantilever at its free end by amplitude D,

$$F = \frac{3EI}{L^3}D \tag{13}$$

with D = Lsin(45^0) = 14.9 μm and $EI = 3\times10^{-23}\,Nm^2$, then $F \sim .1pN$.

Number of haematite nanoparticles:

The number of particles on the surface of the cylindrical cilium can be estimated assuming it covers the surface of a rectangular surface by the product of the number of particles spanning the horizontal distance and the vertical distance, $N_T = N_h N_v$, where $N_h = 2\pi R / d$ and $N_v = L / d$ where R is the radius of cilium and d is the diameter of a nanoparticle. Thus with R = 100 nm, L = 21 μm and d = 130 nm, the number of nanoparticles is estimated to be $N_T = 2\pi RL/d^2 \approx 780$, which represents an upper bound on the number of particles.

References

(1) Evans, B. A.; Shields, A. R.; Carroll, R. L.; Washburn, S.; Falvo, M. R.; Superfine, R. Magnetically Actuated Nanorod Arrays as Biomimetic Cilia. *Nano Lett* **2007,** *7*, 1428-1434.

(2) Evans, B.; Superfine, R. Design Considerations for Magnetically Actuated Biomimetic Cilia. *Biomimetic Based Applications* **2011,** Chapter 17, 473-500.

(3) Landau, L. D.; Pitaevskii, L. P.; Kosevich, A. M.; Lifshitz, E.M. Theory of Elasticity, *3rd Edition.* **1986,** New York: Pergamon Press.

(4) Stoner, E. C.; Wohlfarth, E. P. A Mechanism of Magnetic Hysteresis in Heterogeneous Alloys. *Philos. Trans. R. Soc. London*, Ser. A **1947**, *240*, 559-642.

(5) Flanders, P. J.; Remeika, J. P. Magnetic Properties of Hematite Single Crystals. *Philos. Mag.* **1965,** *11*, 1271-1288.

(6] Bødker, F.; Hansen, M. F.; Koch, C.B.; Lefmann, K.; Mørup, S. Magnetic Properties of Hematite Nanoparticles. *Physical Review B* **2000,** *61*, 6826-6838.

Supporting Figures and Legends

Figure S1

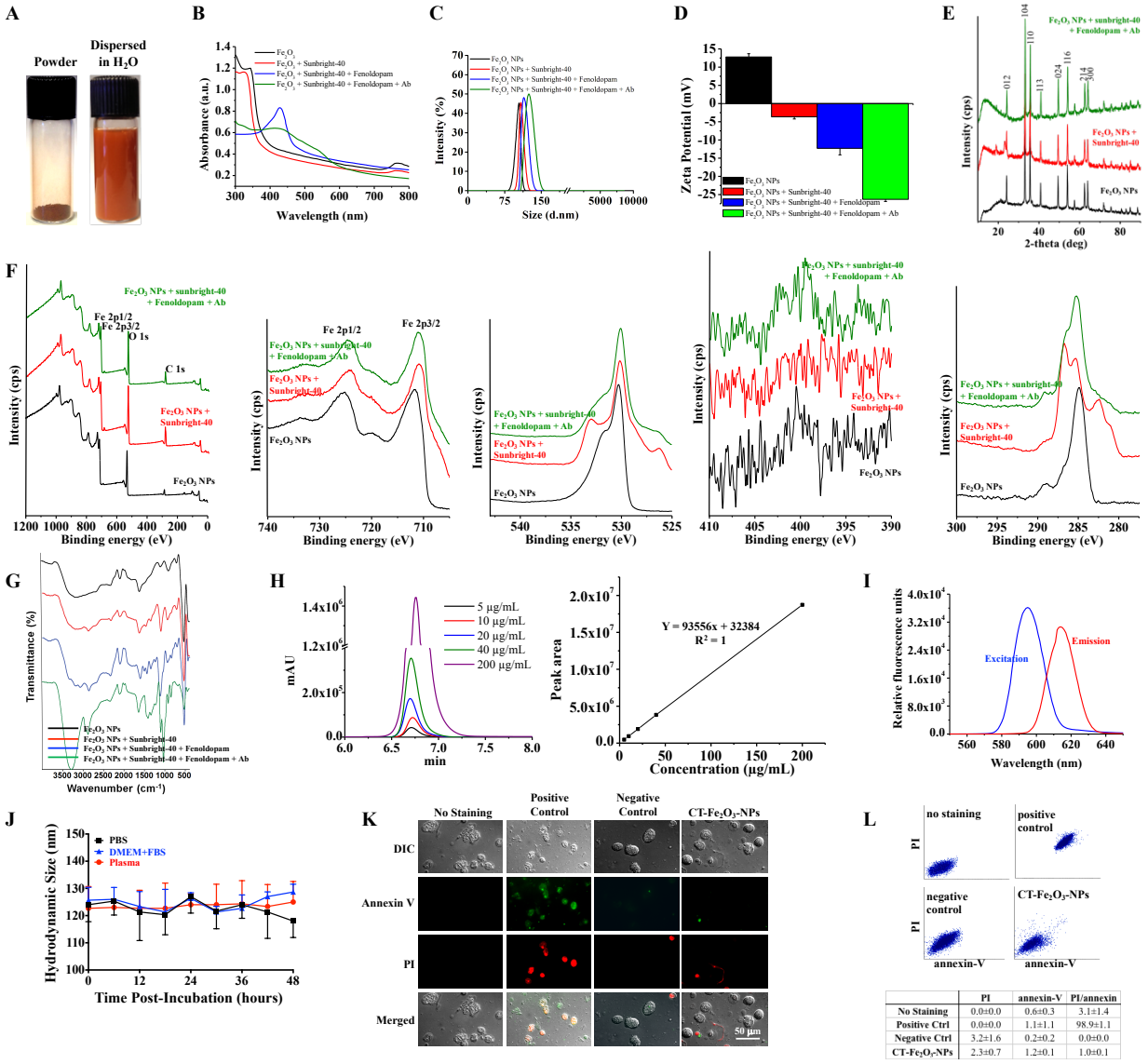

	PI	annexin-V	PI/annexin
No Staining	0.0±0.0	0.6±0.3	3.1±1.4
Positive Ctrl	0.0±0.0	1.1±1.1	98.9±1.1
Negative Ctrl	3.2±1.6	0.2±0.2	0.0±0.0
CT-Fe_2O_3-NPs	2.3±0.7	1.2±0.1	1.0±0.1

Figure S1 | Physical and chemical characterization of functionalized CTNDDSs.

(A) Photograph of the synthesized CT-Fe_2O_3-NPs in powder and dispersed forms.
(B) UV-visible spectra of different steps in the surface functionalization process for Fe_2O_3-NPs in dispersed form.
(C) Hydrodynamic diameter measurements of bare Fe_2O_3-NPs with different surface modifications, as determined by DLS.
(D) ζ-potentials showing the surface charges of bare Fe_2O_3-NPs with different surface modifications.
(E) XRD patterns of bare Fe_2O_3-NPs with different surface modifications.

(F) XPS patterns of bare Fe_2O_3-NPs with different surface modifications showing one complete and several more focused survey spectra, including the Fe 2p, C 1s, N 1s and O 1s spectra.
(G) FTIR spectra showing the infrared signatures of bare Fe_2O_3-NPs with different surface modifications.
(H) The formulation and equilibration of HPLC column and liquid solvent were achieved using known fenoldopam concentrations to obtain a standard approach and fenoldopam retention time. An HPLC calibration curve of fenoldopam (reference standard) is also shown.
(I) Alexa Fluor 594 was successfully conjugated to the antibody, as evidenced by the fluorescence excitation and emission spectra of the NPs.
(J) Hydrodynamic size of NPs dispersed in PBS, DMEM/FBS and plasma.
(K) Cellular toxicity was visualized by DIC/fluorescence imaging. Annexin-V (green) and propidium iodide (PI; red) were used as apoptotic and necrotic markers, respectively.
(L) Toxicity was quantified with flow cytometry. Data are tabulated for annexin-V, PI or annexin-V/PI positive cells for control (no staining), positive control (methanol permeabilization), negative control (no treatment) and NPs treated for 48 hours.

N=3 samples for all experiments.

Figure S2

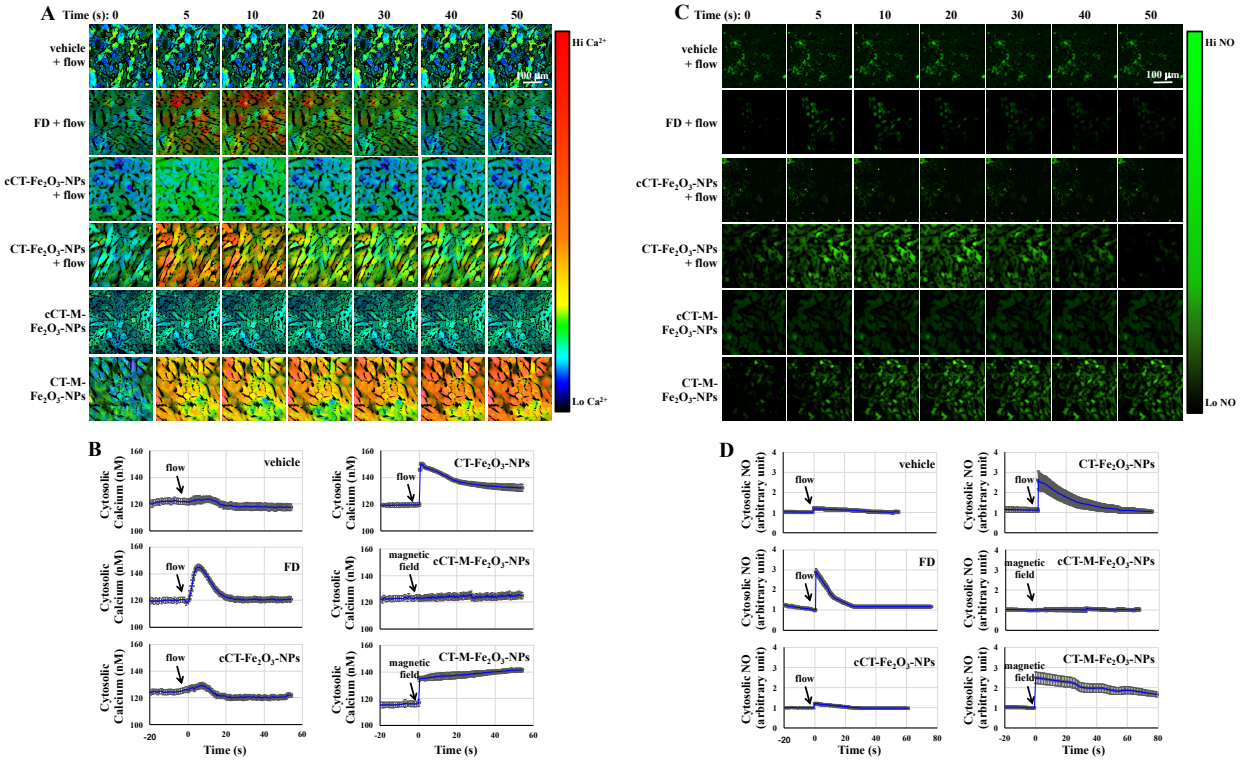

Figure S2 | Intracellular Ca^{2+} and NO measurements.

(A) Cytosolic Ca^{2+} was visualized with the Ca^{2+}-sensitive fluorescent dye Fura-2-AM. Ratiometric images from 340 and 380 nm excitation wavelengths were captured at 50 fps. Numbers on the top of the representative images display the time in seconds (s). A sub-minimal fluid shear of 0.5 dyn/cm^2 was applied to the cells to induce Ca^{2+} flux. The pseudocolour indicates Ca^{2+} levels.

(B) Average cytosolic Ca^{2+} levels (in arbitrary units) were plotted in the line graphs. Arrows indicate the commencement of flow or magnetic force.

(C) Intracellular NO synthesis was visualized with the NO-sensitive fluorescent dye DAF-AM. Effects of sub-minimal fluid shear stress showed greater NO production in treated cells than in control cells. The colour intensity indicates NO levels. Numbers on the top of the representative images display the time in seconds (s). A sub-minimal fluid shear of 0.5 dyn/cm^2 was applied to the cells to induce NO flux.

(D) Average NO levels are shown in the line graphs. Arrows indicate the commencement of flow or magnetic force. In most cases, vehicle treatment (PBS treatment) and CT NPs without loaded drug (cCT-Fe_2O_3-NPs) were used as controls.

N=5 samples per group in each study.

Figure S3

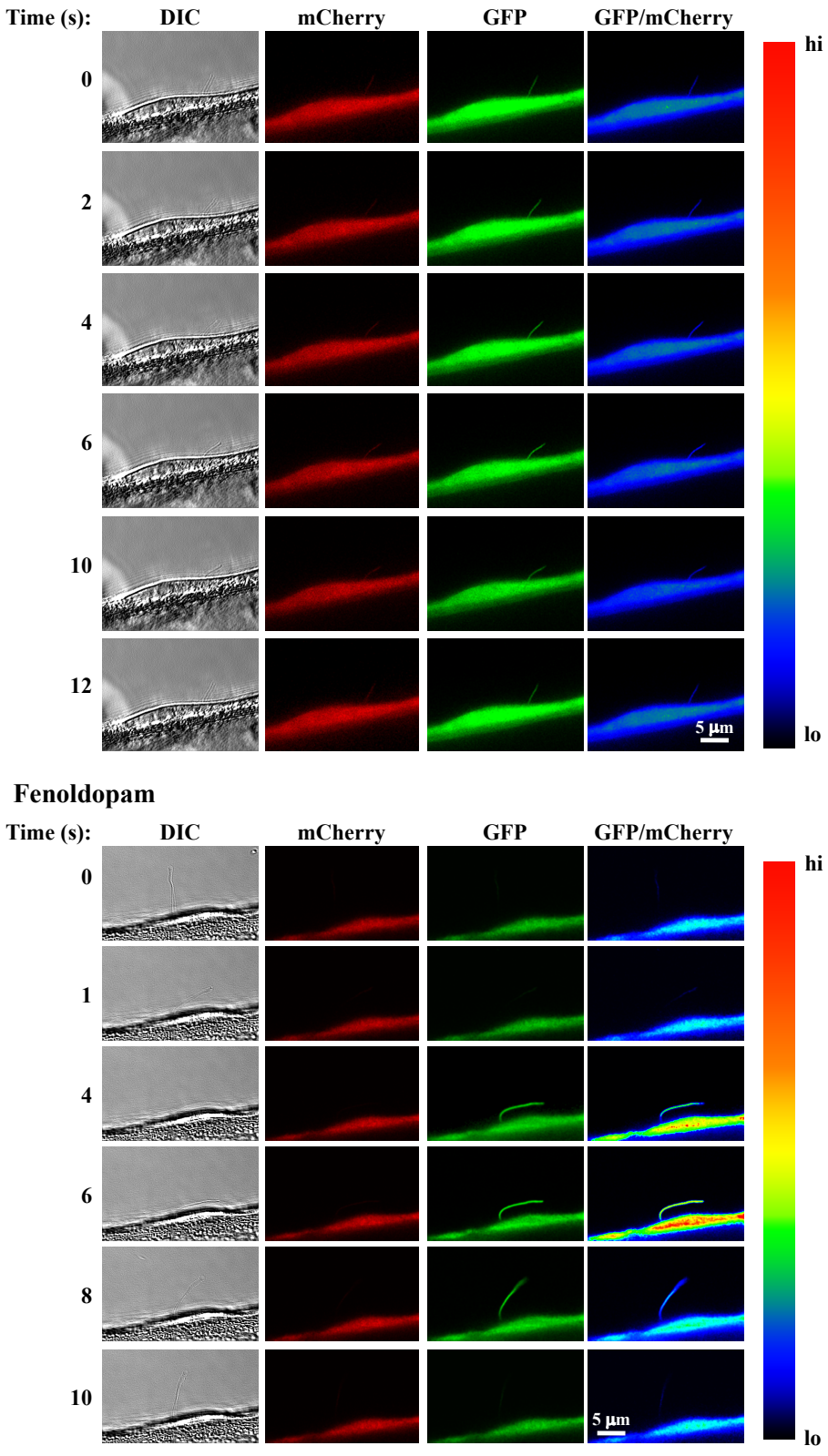
A
Vechicle
Time (s):
DIC
mCherry
GFP
GFP/mCherry
0
2
4
6
10
12
5 µm
hi
lo
B
Fenoldopam
Time (s):
DIC
mCherry
GFP
GFP/mCherry
0
1
4
6
8
10
5 µm
hi
lo

Figure S3 | Single-cell–single-cilium imaging for detecting intraciliary and cytosolic Ca^{2+} levels in control- and fenoldopam (FD)-treated cells challenged with flow.

(A and B) Three sets of images (DIC, mCherry and GFP) were captured at 30 fps. DIC was used to track cilia movement, mCherry was used to normalize motion artefacts, GFP was used to measure changes in Ca^{2+} signals, and the GFP/mCherry ratio (pseudocoloured) indicates the normalized Ca^{2+} level to avoid potential artefacts. The colour bar indicates Ca^{2+} levels. After treatment with PBS (vehicle) or fenoldopam, the cell was challenged with sub-minimal shear stress (0.5 dyn/cm^2). N=4 samples per group in each study. Complete responses (10 seconds) to the shear stress are also shown in Movies S4 and S5.

Figure S4

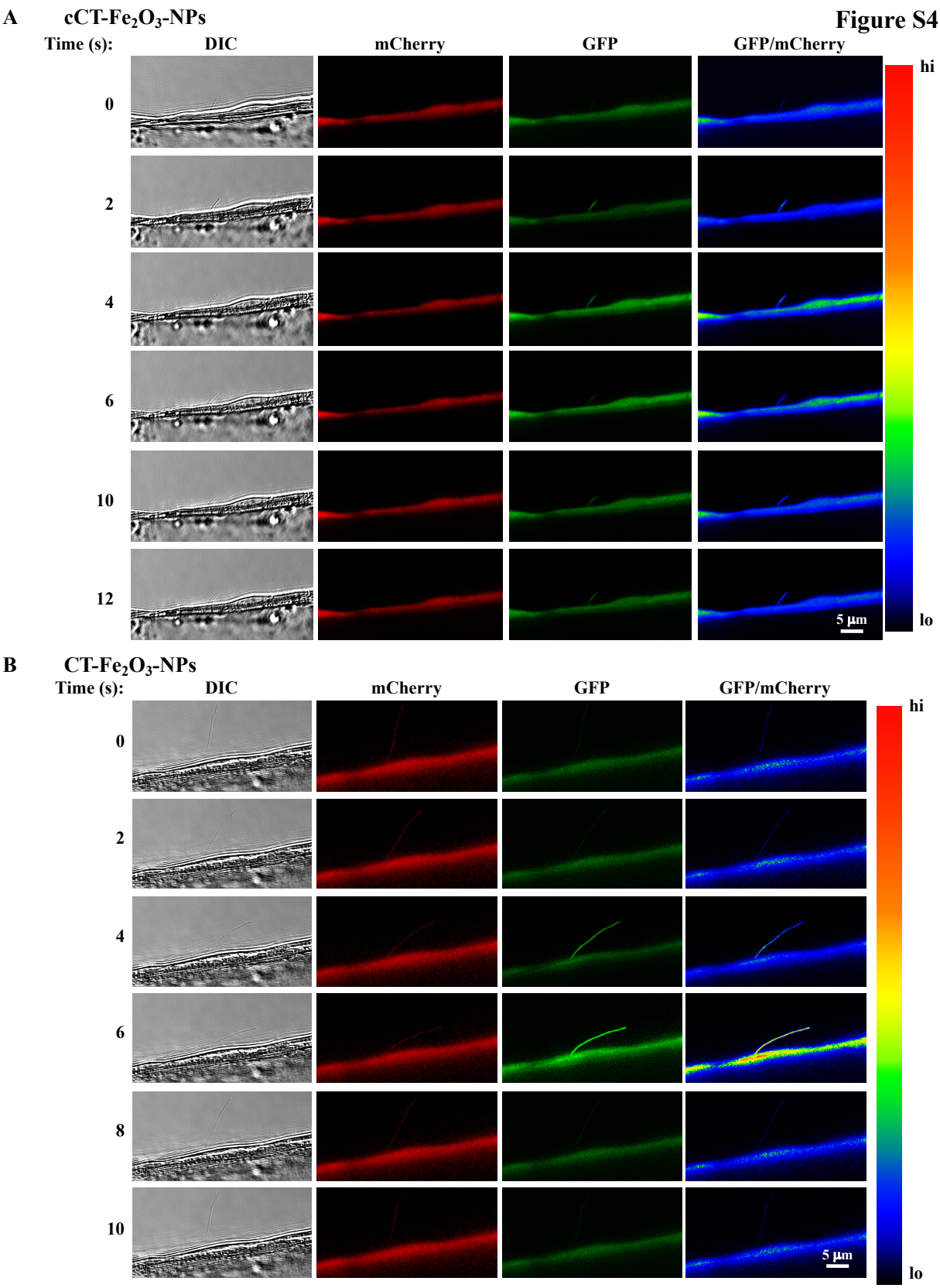
A
cCT-Fe2O3-NPs
Time (s):
DIC
mCherry
GFP
GFP/mCherry
0
2
4
6
10
12
5 µm
hi
lo
B
CT-Fe2O3-NPs
Time (s):
DIC
mCherry
GFP
GFP/mCherry
0
2
4
6
8
10
5 µm
hi
lo

Figure S4 | Single-cell–single-cilium imaging for detecting intraciliary and cytosolic Ca^{2+} levels in cells treated with the cCT-Fe_2O_3-NPs or CT-Fe_2O_3-NPs and challenged with flow.

(A and B) $5HT_6$-mCherry-G-GECO1.0 was expressed in the cilioplasm and cytoplasm. Three sets of images (DIC, mCherry and GFP) were captured at 30 fps. DIC was used to track cilia movement, mCherry was used to normalize motion artefacts, GFP was used to measure changes in Ca^{2+} signals, and the GFP/mCherry ratio (pseudocoloured) indicates normalized Ca^{2+} levels to avoid potential artefacts. The colour bar indicates Ca^{2+} levels. After treatment with the cCT-Fe_2O_3-NPs or CT-Fe_2O_3-NPs, the cell was challenged with sub-minimal shear stress (0.5 dyn/cm^2). N=4 sample per group in each study. Complete responses (10 seconds) to the shear stress are also shown in Movies S6 and S7.

Figure S5

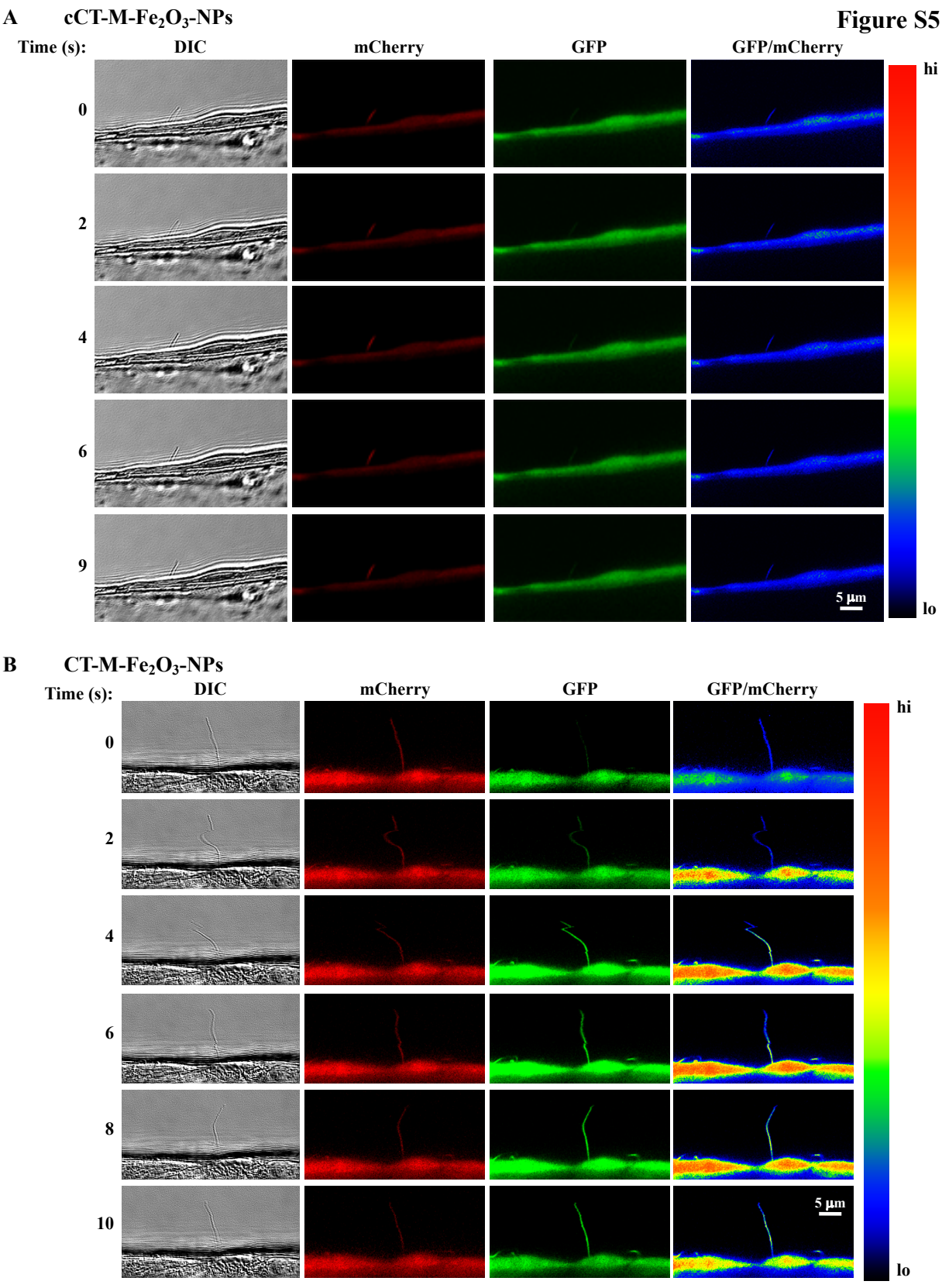
A cCT-M-Fe2O3-NPs
Time (s):
DIC
mCherry
GFP
GFP/mCherry
0
2
4
6
9
5 µm
hi
lo
B CT-M-Fe2O3-NPs
Time (s):
DIC
mCherry
GFP
GFP/mCherry
0
2
4
6
8
10
5 µm
hi
lo

Figure S5 | Single-cell–single-cilium imaging for detecting intraciliary and cytosolic Ca^{2+} levels in cells treated with the cCT-M-Fe_2O_3-NPs or CT-M-Fe_2O_3-NPs and challenged with a magnetic field.

(A and B) $5HT_6$-mCherry-G-GECO1.0 was expressed in the cilioplasm and cytoplasm. Three sets of images (DIC, mCherry and GFP) were captured at 30 fps. DIC was used to track cilia movement, mCherry was used to normalize motion artefacts, GFP was used to measure changes in Ca^{2+} signals, and the GFP/mCherry ratio (pseudocoloured) indicates normalized Ca^{2+} levels to avoid potential artefacts. The colour bar indicates Ca^{2+} levels. After treatment with the cCT-M-Fe_2O_3-NPs or CT-M-Fe_2O_3-NPs, an oscillating magnetic field (1.35 T) was applied. N=4 samples per group in each study. Complete recordings of this experiment are also shown in Movies S8 and S9.

Figure S6

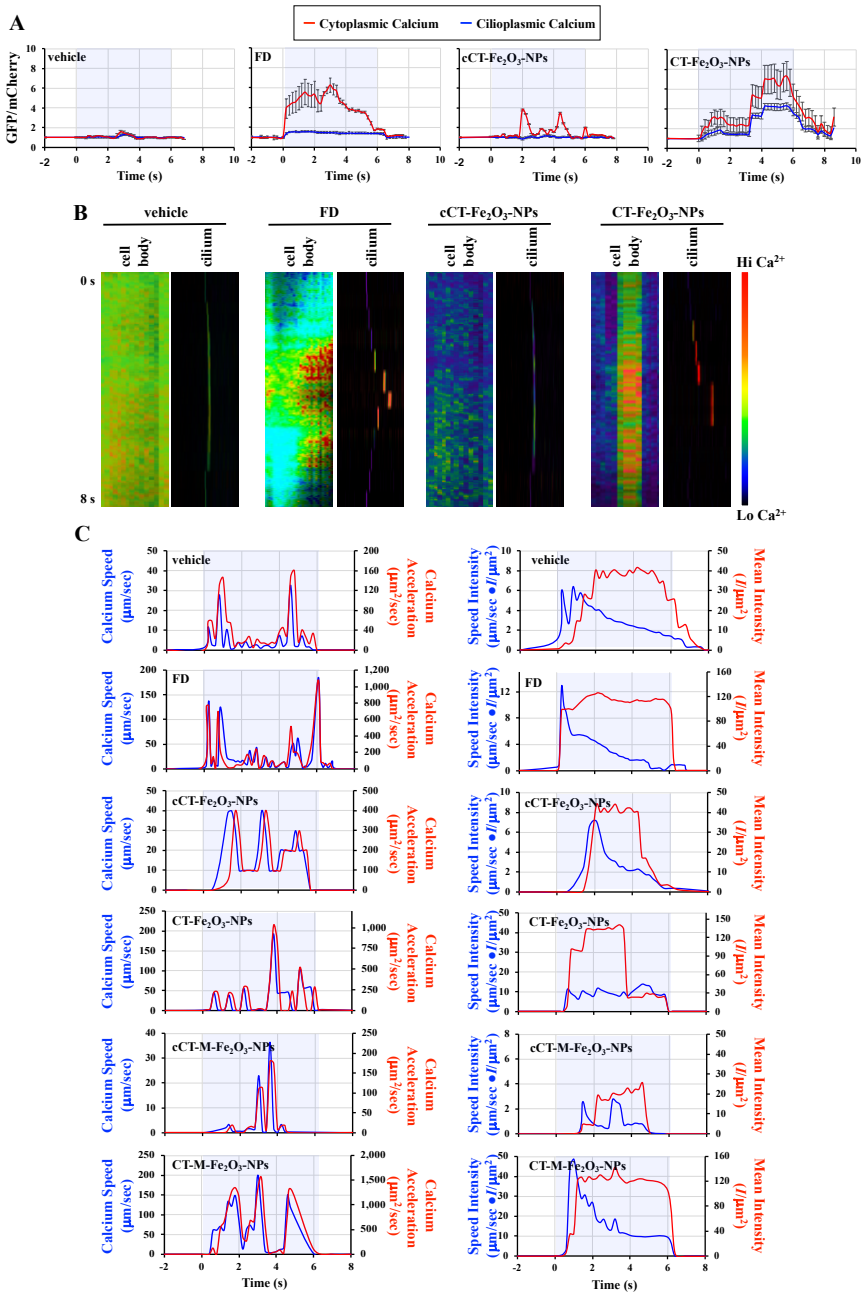

Figure S6 | Kymograph analyses of ciliary and cellular Ca^{+2} traces.

(A) Average cytosolic (red) and cilioplasmic (blue) Ca^{2+} levels are shown in line graphs. The presence of shear stress is represented by the blue background.

(B) Kymograph analyses of Ca^{2+} signaling in the cell body and cilia were performed with controls or with the cCT-Fe_2O_3-NPs or CT-Fe_2O_3-NPs exposed to flow.

(C) Representative traces of changes in Ca^{2+} velocity, acceleration, speed intensity and mean intensity within a single cilium are shown. The presence of shear stress is represented as the blue background. Binary-spot track changes in intraciliary Ca^{2+} are also shown in Movies S4-S9.

In all cases, vehicle (PBS) and the CT-Fe_2O_3-NPs without loaded drug in the absence (cCT-Fe_2O_3-NPs) or presence (cCT-M-Fe_2O_3-NPs) of the magnetic field were used as controls; N=4 samples per group in each study.

Figure S7

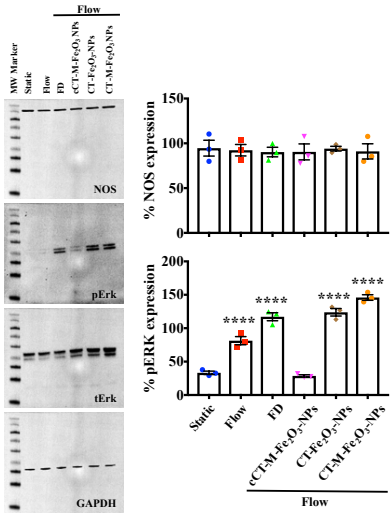

Figure S7 | Effect of CT-Fe_2O_3-NPs on ERK phosphorylation in primary cultured cells.

Representative immunoblots of endothelia show the % levels of NOS and phosphorylated ERK. *, $p<0.05$; **, $p<0.01$; ***, $p<0.001$; and ****, $p<0.0001$ compared with the control (static) group.

Figure S8

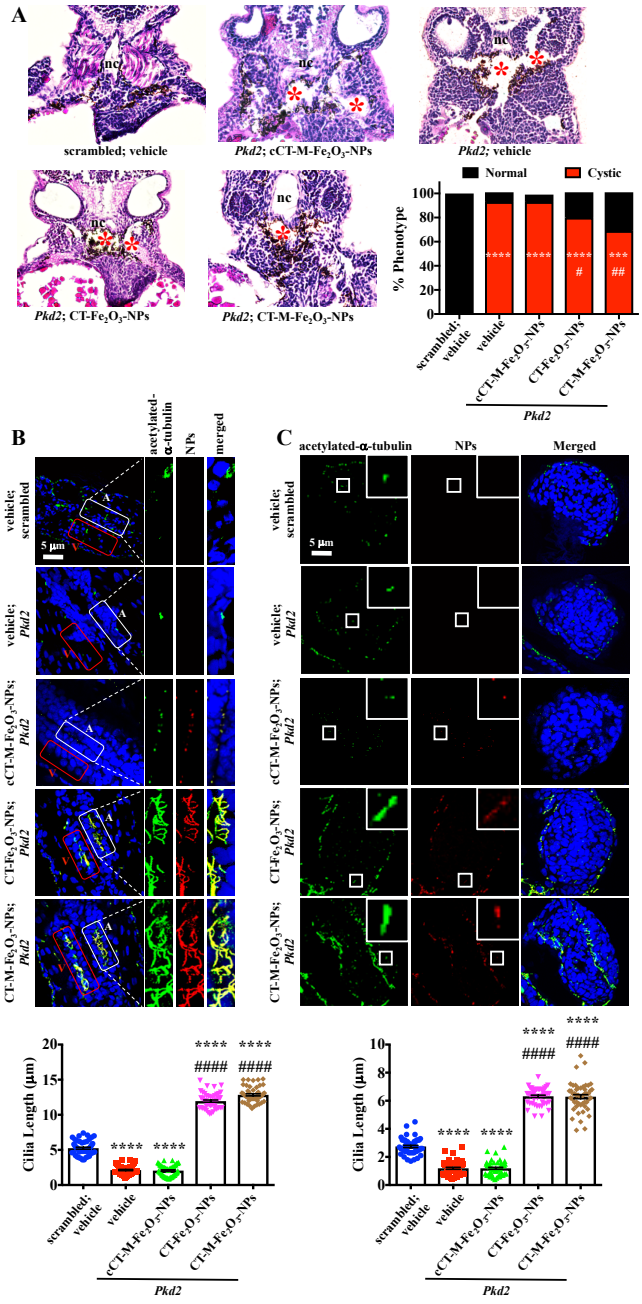

Figure S8 | CT-Fe_2O_3-NPs increase the cilia length in *Pkd2* zebrafish.

(A) H&E sections showing the notochord (nc) and renal nephron in scrambled and *Pkd2* zebrafish treated with PBS, cCT-Fe_2O_3-NPs, CT-Fe_2O_3-NPs or CT-M-Fe_2O_3-NPs. Cystic kidneys are denoted by red asterisks, and the bar graph shows the percentage of zebrafish with dilated or cystic nephrons.

(B) Representative immunofluorescence images of primary cilia in arteries (A; white box) and veins (V; red box) of dorsal vessels are shown. The boxes were further magnified for better visualization. Average cilia length of the blood vessels is shown in the dot-plotted bar graphs.
(C) Representative immunofluorescence images of primary cilia in myocytes throughout the heart are shown. The boxes show one cilium for visualization purposes. Average cilia length in the heart is shown in the dot-plotted bar graphs.

For all immunofluorescence studies, green represents acetylated-α-tubulin (cilia marker), red represents NPs, and blue represents DAPI (nucleus); N=10-50 fish per group in each study; *, $p<0.05$; **, $p<0.01$; ***, $p<0.001$; and ****, $p<0.0001$ compared with the scrambled zebrafish. #, $p<0.05$; ##, $p<0.01$; ###, $p<0.001$; and ####, $p<0.0001$ compared with the *Pkd2* morphants.

Figure S9

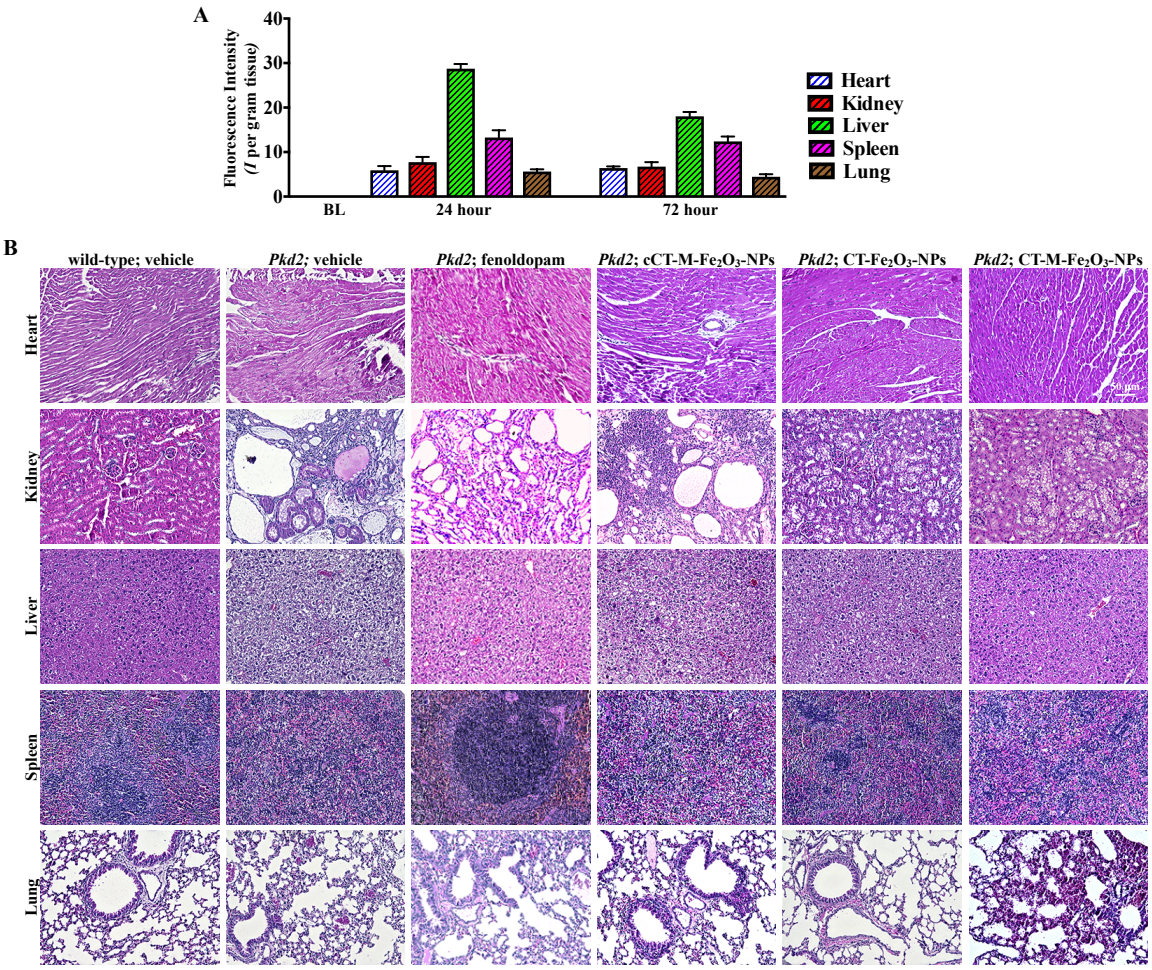

Figure S9 | Distribution and toxicology analyses of CT-Fe_2O_3-NPs.

(A) CT-Fe_2O_3-NPs fluorescence was quantified in major visceral organs to determine their bio-distribution at 24- and 72-hours after the intravenous injection. Mice that did not receive an injection were used as a baseline (BL).

(B) A histopathological analysis of major visceral organs from *Pkd2* mice performed using standard H&E staining did not reveal apparent signs of CT NP toxicity.

N=5 mice per group in each study.

Table S1

	wild-type			*Pkd2*		
	vehicle	**epinephrine**	**diltiazem**	**vehicle**	**epinephrine**	**diltiazem**
HR (beat/min)	143±14	209±15	72±19	134±17	227±17	76±9
ESPVR (mmHg/μL)	5.0±0.04	12.4±3.25	1.6±0.12	3.78±0.07	8.02±2.32	2.10±0.28
EDPVR (mmHg/μL)	0.14±0.01	0.13±0.01	0.18±0.01	0.13±0.01	0.13±0.01	0.13±0.01
dP/dtmax (mmHg/s)	5408±52	16013±524	2775±501	6285±96	14480±453	3475±293
dP/dtmin (mmHg/s)	-1765±130	-3127±85	-1294±129	-1735±97	-3096±82	-1419±281
LV Pmax (mmHg)	50.1±0.5	80.1±5.1	38.2±0.1	58.2±0.1	72.4±7.3	38.6±3.3
LV ESP (mmHg)	37.5±0.4	60.0±3.8	23.1±0.4	43.6±0.1	54.3±5.4	29.0±2.5
LV EDP (mmHg)	5.4±0.4	5.2±0.1	4.8±2.4	5.4±0.1	5.2±0.1	5.3±0.1
LV ESV (μL)	10.1±0.1	6.8±0.2	12.7±0.6	15.4±0.3	10.1±1.8	18.9±1.2
LV EDV (μL)	40.3±0.1	41.2±0.5	40.0±0.1	40.1±0.1	40.9±0.2	40.3±0.2
SV (μL)	30.3±0.1	34.3±1.9	14.0±0.7	24.7±0.3	30.9±2.1	21.4±1.3
SW (mmHg•μL)	1345±38	2566±394	365±83	1304±17	2078±121	715±17
EF (%)	74.8±0.1	83.3±3.6	52.5±2.7	61.6±0.7	75.4±4.6	53.1±3.1
CO (μL/min)	4338±21	7158±299	1261±139	3310±51	7017±703	1928±118

HR, heart rate; ESPVR and EDPVR, end-systolic and end-diastolic pressure volume relation, respectively; dP/dtmax and dP/dtmin, maximum rate of left ventricle (LV) pressure rise and fall, respectively; Pmax, systolic pressure; ESP, end-systolic pressure; EDP, end-diastolic pressure; ESV, end-systolic volume; EDV, end-diastolic volume; SV, stroke volume; SW, stroke work; EF, ejection fraction; CO, cardiac output.

Table S2

	***Pkd2;* Fenoldopam**		
	vehicle	**epinephrine**	**diltiazem**
HR (beat/min)	136±26	216±47	94±11
ESPVR (mmHg/μL)	4.6±0.04	9.8±0.88	2.21±0.03
EDPVR (mmHg/μL)	0.13±0.01	0.16±0.01	0.14±0.01
dP/dtmax (mmHg/s)	7524±71	17130±239	4020±642
dP/dtmin (mmHg/s)	-1625±27	-3844±278	-1537±97
LV Pmax (mmHg)	69.7±0.7	85.6±1.2	44.7±0.7
LV ESP (mmHg)	52.2±0.5	64.2±0.9	35.5±0.5
LV EDP (mmHg)	5.0±0.1	6.4±0.5	5.7±0.2
LV ESV (μL)	15.0±0.1	8.9±0.8	20.2±0.1
LV EDV (μL)	40.0±0.1	39.9±0.1	40.0±0.4
SV (μL)	25.0±0.1	31.0±0.8	19.8±0.3
SW (mmHg•μL)	1616±70	2569±53	772±10
EF (%)	62.5±0.2	77.7±2.0	49.5±0.3
CO (μL/min)	3402±92	6707±373	1783±32

HR, heart rate; ESPVR and EDPVR, end-systolic and end-diastolic pressure volume relation, respectively; dP/dtmax and dP/dtmin, maximum rate of left ventricle (LV) pressure rise and fall, respectively; Pmax, systolic pressure; ESP, end-systolic pressure; EDP, end-diastolic pressure; ESV, end-systolic volume; EDV, end-diastolic volume; SV, stroke volume; SW, stroke work; EF, ejection fraction; CO, cardiac output.

Table S3

	Pkd2; CT-Fe_2O_3-NPs			*Pkd2;* CT-M-Fe_2O_3-NPs		
	vehicle	**epinephrine**	**diltiazem**	**vehicle**	**epinephrine**	**diltiazem**
HR (beat/min)	143±16	239±13	92±15	117±19	252±34	82±9
ESPVR (mmHg/μL)	4.4±0.09	9.3±1.31	2.2±0.25	4.6±0.22	10.5±2.63	1.9±0.40
EDPVR (mmHg/μL)	0.14±0.01	0.14±0.01	0.04±0.01	0.12±0.01	0.13±0.01	0.12±0.01
dP/dtmax (mmHg/s)	5900±38	15499±857	3454±137	5813±178	15283±940	3348±180
dP/dtmin (mmHg/s)	-1767±43	-3498±159	-1497±62	-1603±365	-3146±186	-1290±159
LV Pmax (mmHg)	54.6±0.4	77.5±4.3	39.4±1.5	53.8±1.6	76.4±4.7	37.2±2.0
LV ESP (mmHg)	41.0±0.3	58.1±3.2	28.8±1.1	40.4±1.2	57.3±3.5	27.9±1.5
LV EDP (mmHg)	5.4±0.1	5.8±0.3	5.5±0.1	5.0±0.3	5.2±0.1	4.8±0.1
LV ESV (μL)	12.4±0.3	8.5±0.8	17.8±2.3	11.7±0.9	7.9±1.3	21.0±3.0
LV EDV (μL)	40.4±0.1	40.8±0.6	40.8±0.6	40.1±0.2	40.8±0.5	40.4±0.1
SV (μL)	27.9±0.3	32.3±0.4	23.0±2.6	28.4±1.0	32.8±1.8	19.5±3.1
SW (mmHg•μL)	1372±41	2313±78	755±172	1388±83	2337±69	632±25
EF (%)	69.1±0.8	79.1±1.7	56.3±5.9	70.7±2.3	80.5±3.5	48.2±7.8
CO (μL/min)	3989±45	7718±566	2071±401	3334±201	8279±122	1754±279

HR, heart rate; ESPVR and EDPVR, end-systolic and end-diastolic pressure volume relation, respectively; dP/dtmax and dP/dtmin, maximum rate of left ventricle (LV) pressure rise and fall, respectively; Pmax, systolic pressure; ESP, end-systolic pressure; EDP, end-diastolic pressure; ESV, end-systolic volume; EDV, end-diastolic volume; SV, stroke volume; SW, stroke work; EF, ejection fraction; CO, cardiac output.

Table S4

	IFT88			*IFT88;* Fenoldopam		
	vehicle	**epinephrine**	**diltiazem**	**vehicle**	**epinephrine**	**diltiazem**
HR (beat/min)	140±23	213±24	101±17	144±32	241±22	104±20
ESPVR (mmHg/μL)	4.3±0.3	10.0±1.2	2.0±0.01	5.4±0.7	10.0±1.1	2.1±0.1
EDPVR (mmHg/μL)	0.12±0.01	0.16±0.02	0.14±0.01	0.13±0.01	0.13±0.01	0.13±0.01
dP/dtmax (mmHg/s)	7142±429	16797±383	3635±157	7819±140	17206±578	3619±111
dP/dtmin (mmHg/s)	-1538±41	-3795±548	-1475±218	-1658±190	-3180±120	-1372±330
LV Pmax (mmHg)	66.1±4.0	84.0±2.0	40.4±0.2	72.4±1.3	56.0±0.3	40.2±0.1
LV ESP (mmHg)	49.6±3.0	63.0±1.5	30.3±0.1	54.3±1.0	64.5±0.2	30.2±0.1
LV EDP (mmHg)	4.7±0.1	6.3±1.0	5.5±0.4	5.1±0.1	5.3±0.2	5.1±0.1
LV ESV (μL)	15.5±0.3	8.7±1.1	20.0±0.2	13.8±1.4	8.7±0.9	19.4±0.7
LV EDV (μL)	40.4±0.2	40.2±0.1	40.1±0.1	40.1±0.1	40.2±0.1	40.0±0.1
SV (μL)	24.9±0.1	35.5±1.0	20.1±0.1	26.3±1.4	31.4±0.8	20.6±0.7
SW (mmHg•μL)	1528±63	2448±121	701±97	1767±56	2538±16	725±20
EF (%)	61.6±0.4	78.5±2.7	50.1±0.1	65.5±3.5	78.2±2.2	51.6±1.7
CO (μL/min)	3478±121	6717±247	1808±71	3780±437	7590±176	1857±137

HR, heart rate; ESPVR and EDPVR, end-systolic and end-diastolic pressure volume relation, respectively; dP/dtmax and dP/dtmin, maximum rate of left ventricle (LV) pressure rise and fall, respectively; Pmax, systolic pressure; ESP, end-systolic pressure; EDP, end-diastolic pressure; ESV, end-systolic volume; EDV, end-diastolic volume; SV, stroke volume; SW, stroke work; EF, ejection fraction; CO, cardiac output.

Table S5

	IFT88; cCT-Fe_2O_3-NPs			*IFT88;* CT-M-Fe_2O_3-NPs		
	vehicle	**epinephrine**	**diltiazem**	**vehicle**	**epinephrine**	**diltiazem**
HR (beat/min)	153±34	257±30	108±25	166±26	266±21	106±34
ESPVR (mmHg/μL)	4.5±0.1	10.0±1.5	2.1±0.1	4.9±0.1	10.1±1.1	2.2±0.1
EDPVR (mmHg/μL)	0.16±0.02	0.19±0.04	0.18±0.03	0.15±0.01	0.14±0.01	0.21±0.04
dP/dtmax (mmHg/s)	7754±186	17428±497	3741±110	7615±168	17190±199	3999±159
dP/dtmin (mmHg/s)	-2045±263	-4648±882	-1914±561	-1981±180	-3439±229	-2227±902
LV Pmax (mmHg)	71.8±1.7	87.1±2.5	41.6±1.2	70.5±1.6	86.0±0.5	43.3±1.8
LV ESP (mmHg)	53.8±1.3	65.4±1.9	31.2±0.9	52.9±1.5	64.5±1.4	32.5±1.3
LV EDP (mmHg)	6.3±0.8	7.7±1.5	7.1±1.0	6.1±0.6	5.7±0.4	8.2±1.7
LV ESV (μL)	16.0±0.6	9.0±1.0	20.2±0.1	14.5±0.5	8.7±0.9	19.4±0.6
LV EDV (μL)	40.1±0.1	40.7±0.4	40.1±0.1	41.2±0.4	40.0±1.3	40.1±0.1
SV (μL)	24.2±0.6	31.7±0.7	19.9±0.1	26.7±0.4	31.3±1.9	20.7±0.6
SW (mmHg•μL)	1582±45	2519±113	688±45	1720±14	2507±67	724±77
EF (%)	60.2±1.5	77.9±2.4	49.7±0.2	64.9±0.9	78.1±2.8	51.5±1.4
CO (μL/min)	3711±198	8147±212	1794±12	4439±103	8317±401	1859±19

HR, heart rate; ESPVR and EDPVR, end-systolic and end-diastolic pressure volume relation, respectively; dP/dtmax and dP/dtmin, maximum rate of left ventricle (LV) pressure rise and fall, respectively; Pmax, systolic pressure; ESP, end-systolic pressure; EDP, end-diastolic pressure; ESV, end-systolic volume; EDV, end-diastolic volume; SV, stroke volume; SW, stroke work; EF, ejection fraction; CO, cardiac output.

Table S6

	IFT88; CT-Fe_2O_3-NPs		
	vehicle	**epinephrine**	**diltiazem**
HR (beat/min)	145±39	243±32	104±24
ESPVR (mmHg/μL)	5.1±0.4	9.7±1.4	2.2±0.1
EDPVR (mmHg/μL)	0.13±0.01	0.14±0.01	0.21±0.04
dP/dtmax (mmHg/s)	7966±203	17265±184	3966±105
dP/dtmin (mmHg/s)	-1738±97	-3483±239	-2252±806
LV Pmax (mmHg)	73.8±1.9	86.3±0.9	44.1±1.2
LV ESP (mmHg)	55.3±1.4	64.7±0.7	33.1±0.9
LV EDP (mmHg)	5.4±0.3	5.8±0.4	8.3±1.5
LV ESV (μL)	14.5±0.8	9.3±1.3	19.8±0.7
LV EDV (μL)	40.3±0.3	40.2±0.1	40.5±0.2
SV (μL)	25.9±0.6	30.9±1.2	20.6±0.6
SW (mmHg•μL)	1769±40	2488±62	737±63
EF (%)	64.1±1.7	76.9±3.1	50.9±1.6
CO (μL/min)	3754±244	7513±378	1856±140

HR, heart rate; ESPVR and EDPVR, end-systolic and end-diastolic pressure volume relation, respectively; dP/dtmax and dP/dtmin, maximum rate of left ventricle (LV) pressure rise and fall, respectively; Pmax, systolic pressure; ESP, end-systolic pressure; EDP, end-diastolic pressure; ESV, end-systolic volume; EDV, end-diastolic volume; SV, stroke volume; SW, stroke work; EF, ejection fraction; CO, cardiac output.

Table S7: Safety evaluation of CT-M-Fe_2O_3-NPs treatment *in vivo* was assessed by analyzing hematology and biochemistry parameters.

Analytes	Vehicle	CT-M-Fe_2O_3-NPs
WBC ($\times10^9$/L)	9.9±2.4	9.4±3.1
LYM ($\times10^9$/L)	9.1±2.6	9.0±2.9
MON ($\times10^9$/L)	0.09±0.01	0.08±0.03
NEU ($\times10^9$/L)	0.41±0.19	0.45±0.23
RBC ($\times10^{12}$/L)	9.94±0.3	9.82±0.4
HGB (g/dL)	13.9±1.2	13.8±1.8
HCT (%)	42.1±0.6	42.0±0.8
MCV (fl)	43.0±5.2	41.3±4.3
ALB (g/dL)	3.5±0.7	3.2±0.9
ALP (U/L)	47±38	49±27
ALT (U/L)	34±1.5	29±1.9
AMY (U/L)	801±46	803±38
TBIL (mg/dL)	0.3±0.2	0.3±0.2
CA (mg/dL)	10.2±0.9	8.7±0.6
PHOS (mg/dL)	7.9±1.9	7.8±2.3
CRE (mg/dL)	0.2±0.07	0.3±0.1
GLU (mg/dL)	304±53	287±43
Na^+ (mmol/L)	163±2.4	155±1.8
K^+ (mmol/L)	4.4±0.7	4.5±0.7
TP (g/dL)	5.1±0.4	4.7±0.9
GLOB (g/dL)	1.7±0.6	1.2±0.2

WBC, white blood cell; LYM, lymphocyte; MON, monocyte; NEU, neutrophil; RBC, red blood cell; HGB, hemoglobin; HCT, hematocrit; MCV, mean corpuscular volume; ALB, albumin; ALP, alkaline phosphatase; ALT, alanine aminotransferase; AMY, amylase; TBIL, total bilirubin; CA, calcium; PHOS, phosphorus; CRE, creatinine; GLU, glucose; Na^+, sodium; K^+, potassium; TP, total protein; GLOB, globulin.

Resources Table

Reagents or Resources	Sources	Identifiers
Antibodies		
Anti-Dopamine D_5 Receptor Antibody	EMD Millipore	Cat#324408
Monoclonal Anti-α-Tubulin Antibody	Sigma	RRID: AB_477593
p44/42 MAPK (Erk1/2) Antibody	Cell Signaling Technology	RRID: AB_330744
p44/42 MAP kinase (phosphorylated Erk1/2) Antibody	Cell Signaling Technology	RRID: AB_331646
Mouse Anti-eNOS Monoclonal Antibody	Abcam	RRID: AB_1310183
Rabbit Anti-GAPDH Monoclonal Antibody	Cell Signaling Technology	RRID: AB_561053
Anti-rabbit IgG, HRP-linked Antibody	Cell Signaling Technology	RRID: AB_2099233
Anti-mouse IgG, HRP-linked Antibody	Cell Signaling Technology	RRID: AB_330924
Fluorescein Horse Anti-Mouse IgG Antibody	Vector Laboratories	Cat#FI-2000
Texas Red® Horse Anti-Mouse IgG Antibody	Vector Laboratories	Cat#TI-2000
Chemicals, Peptides, and Recombinant Proteins		
Ferric nitrate nonahydrate	Amresco	Cas#7782-61-8
Ammonia solution 25 %	EMD Millipore	Cat#105428
SUNBRIGHT® OE-080CS	NOF Corporation	Lot#M152565
Dimethyl sulfoxide	Thermo Fisher Scientific	Cat#20688
Fenoldopam mesylate	United States Pharmacopeia	Cat#1269458
Alexa Fluor™ 594 C5 Maleimide	Thermo Fisher Scientific	Cat#A10256
VECTASHIELD HardSet Antifade Mounting Medium with DAPI	Vector Laboratories	Cat#H-1500
Formvar	Electron Microscopy Sciences	Cat#15800
Paraformaldehyde 16%	Electron Microscopy Sciences	Cat#15710-SP-500
Triton™ X-100	Fisher Scientific	Cas#9002-93-1
Fura-2 (AM)	Teflabs	Cat#0103
DAF-2 diacetate	Cayman Chemical	Cas#205391-02-2

jetPRIME®	VWR	Cat#89129-920
Protease Inhibitor Cocktail	Medchemexpress	Cat#HY-K0011
Rp-8-pCPT-cGMPS sodium salt	Enzo life sciences	Cas#153660-04-9
Epinephrine	Vetone	NDC: 13985-493-34
Diltiazem Hydrochloride	Akorn Pharmaceuticals	NDC: 17478-937-25
Ketamine Hydrochloride	Spectrum chemical	Cat#K1068
Xylazine Hydrochloride	Spectrum chemical	Cat#X1067
HEPARIN Sodium	Sagent Pharmaceuticals	NDC: 25021-400-10
Sodium chloride	Sigma	Cas#7647-14-5
Potassium chloride	Fisher Scientific	Cas#7447-40-7
Sodium dihydrogen phosphate monohydrate	VWR	Cas#10049-21-5
Calcium chloride	Sigma	Cat#449709
Magnesium chloride	Sigma	Cas#7786-30-3
Sodium Bicarbonate	Fisher scientific	Cat#S233-500
(±)-SKF-38393 hydrochloride	Enzo life sciences	Cas# 62717-42-4
HISTOCHOICE® MOUNTING MEDIA	Amresco	Cat#H157
Eosin Phloxine	VWR	Cat#10143-140
Alcohol, 100%	Fisher Scientific	Cas# 64-17-5
Neutral Buffered Formalin (10%)	Fisher Scientific	Cat#22-046-361
Xylene	VWR	Cat#89370-088
Formic acid	Amresco	Cas#64-18-6
Critical Commercial Assays		
Prussian Blue Reagent Pack	Biopal.Inc	Cat#CL-01-50
MycoAlertTM Mycoplasma Detection Kit	Lonza	Cat# LT07-218
Dead Cell Apoptosis Kit with Annexin V FITC and PI, for flow cytometry	Thermo Fisher Scientific	Cat#V13242
IHC antigen retrieval reagent	Enzo life sciences	Cat#ADI-950-271-0500
Collagen I	Corning	Ref#54236
Cyclic GMP ELISA Kit	Cayman chemical	Item#581021
Urea Nitrogen (BUN) Colorimetric Detection Kit	Arbor assays	Cat#K024-H1
Nitrate/Nitrite Colorimetric Assay Kit	Cayman chemical	Item#780001

Masson's Trichrome Stain Kit	Polysciences,Inc	Cat#25088-100
Experimental Models: Cell Lines		
LLC-PK1	ATCC	CL-101
Experimental Models: Organisms/Strains		
AB zebrafish	Eugene	ID#ZDB-GENO-960809-7
Tie2Cre	The Jackson Laboratory	Stock#008863
Pkd2$^{flox/flox}$	Brigham and Women's Hospital (Dr. Jing Zhou)	MTA#A223329
IFT88$^{flox/flox}$	University of Alabama, Birmingham (Dr. Bradley Yoder); Jackson Laboratory	MTA#A008749
Oligonucleotides		
5′-CCT CTT ACC TCA GTT ACA ATT TAT A-3′	Gene tools [last accessed on June 2015]	http://www.gene-tools.com
5′-AGG ACG AAC GCG ACT GGG CTC ATC-3′	Gene tools [last accessed on June 2015]	http://www.gene-tools.com
Recombinant DNA		
5HT6-mCherry-G-GECO1.0	Addgene	Cat#47500
Software and Algorithms		
Prism 7	GraphPad Software [last accessed on December 2018]	https://www.graphpad.com /scientific- software/prism/
Advanced Research	NIS-Elements [last accessed on June 2018]	https://www.nikoninstruments.com/Products/Software/NIS-Elements-Advanced-Research/NIS-Elements-Viewer
Image Lab Ver 5.1	Bio-Rad [last accessed on June 2018]	http://www.bio-rad.com/en-al/product/image-lab-software
iox2, data acquisition & analysis software	Emka Technologies [last accessed on June 2018]	https://www.emka.fr/product/iox2-software/

LabSolutions	Shimadzu [last accessed on June 2018]	https://www.shimadzu.com/an/data-net/labsolutions/labsol-8.html
Other		
Dialysis membrane	Spectrum Labs	Cat#131192
Alnico Cylindrical Magnet	VWR	Cat#470149-700
P720 Peristaltic Pumps	Instech [last accessed on January 2014]	https://www.instechlabs.com/products/pumps/peristaltic/p720
Mouse heart cannula 20 gauge (straight)	Radnoti	Cat#130163-20
Mouse heart cannula 20 gauge (bent)	Radnoti	Cat#130164-20